nature chemistry

Article

https://doi.org/10.1038/s41557-025-01953-2

Covalent organic frameworks as infinite building units for metal–organic frameworks with compartmentalized pores

Received: 12 February 2025

Accepted: 19 August 2025

Published online: 7 October 2025

Check for updates

Bo Liu[1,2,4], Yichen Wu[3,4], Linxia Wang[1], Hai-Long Jiang[2] ✉ & Qiaowei Li[3] ✉

Metal–organic frameworks typically rely on discrete molecules as building units, and creating frameworks featuring continuous organic or inorganic subnet moieties, such as chains and layers, is challenging. While all-inorganic subnets have been used as units with infinite connectivity, the intrinsic disorder in organic chains and layers hinders their role as well-defined building blocks for reticular materials. Here we report the one-pot synthesis of a series of Zr_6O_8-based or Hf_6O_8-based metal–organic frameworks that feature boroxine-based one-dimensional and two-dimensional covalent organic frameworks—chains with diverse conformations and layers with specific topology, respectively—as the organic components. The spatial compatibility between the constituents locks the infinite organic units into patterned arrangements and thus generates metal–organic frameworks with distinct structural entities and pore environments in separate sections along specific directions. The coexistence of extended covalent organic frameworks and discrete inorganic units, side by side and yet independent of each other, leads to high structural compartmentalization in space.

Reticular chemistry relies on linking various building units into extended structures through strong bonds[1]. Designing building units with specific geometries and applying diverse linkage chemistry to interconnect them constitute the key steps of reticular synthesis[2–5]. Building units such as single metal ions, polynuclear metal–oxo clusters, carboxylates and azolates have been employed to construct numerous metal–organic frameworks (MOFs) in last three decades[6–13]. While most units are discrete shapes, infinite inorganic chains and layers have also been used as framework structures, collectively termed extended inorganic hybrids[14]. These include one-dimensional (1D) and two-dimensional (2D) metal oxides and chalcogenides[15–23], halides[24,25], phosphates[26] and so on, which offer the advantage of unlimited connectivity. By contrast, integrating organic chains and layers as building units into the frameworks remains a pressing challenge because polymeric structures are typically disordered, and thus their perfect alignment with other rigid building units across the periodic space is not feasible.

Covalent organic frameworks (COFs) provide an infinite and precise arrangement of unlimited organic units[27–34]. Theoretically, 1D, 2D and even three-dimensional (3D) COFs could serve as organic linkers with infinite connectivity for the MOF construction[35]. However, incorporating COFs directly as linkers into MOFs, with all components held together by strong bonds in one crystal, is a daunting task because COFs are intrinsically insoluble and lack binding groups that can further coordinate with metal ions. One-pot synthesis, while circumventing the solubility issue, requires (1) the judicious design of multiple constituents that exhibit high spatial and chemical compatibility and (2) the sophisticated manipulation of both covalent and coordinative

[1]College of Chemistry & Pharmacy, Northwest A&F University, Yangling, China. [2]Hefei National Research Center for Physical Sciences at the Microscale, Department of Chemistry, University of Science and Technology of China, Hefei, China. [3]Department of Chemistry, Collaborative Innovation Center of Chemistry for Energy Materials, and Shanghai Key Laboratory of Molecular Catalysis and Innovative Materials, Fudan University, Shanghai, China. [4]These authors contributed equally: Bo Liu, Yichen Wu. ✉e-mail: jianglab@ustc.edu.cn; qwli@fudan.edu.cn

https://doi.org/10.1038/s41557-025-01953-2

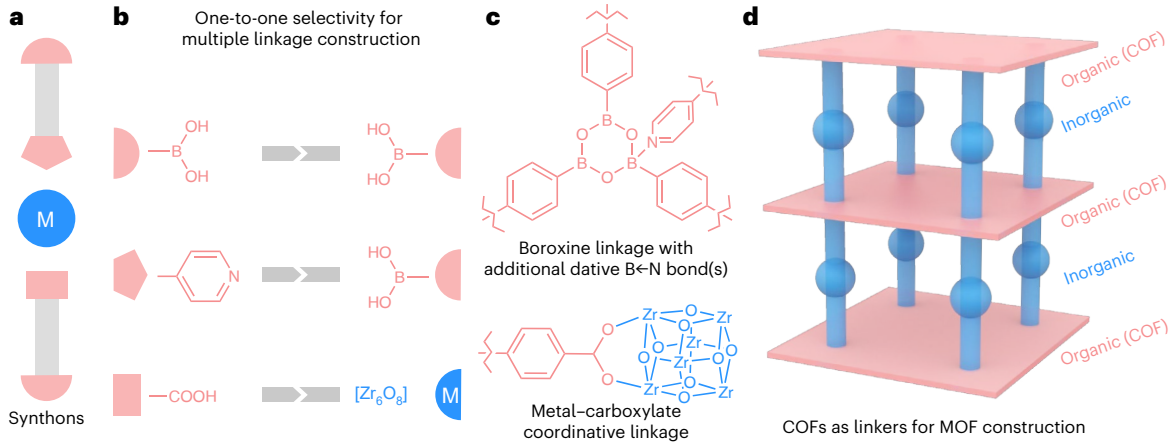

Fig. 1 | Strategies to construct infinite organic linkers and the resulting MOFs. **a**, Organic synthons with different binding groups at the ends and metal ions (M) are employed. **b**, The one-to-one selectivity between the binding moieties, such as boronic acid with boronic acid, pyridyl with boronic acid and carboxylate with a $[Zr_6O_8]$ cluster, enables the construction of multiple linkages within one structure in a concurrent manner. **c**, Two kinds of linkages exist in the reported structures: a boroxine linkage with or without additional dative B←N bonds and a Zr–carboxylate coordinative linkage. **d**, This strategy creates MOFs with COFs as the infinite linkers.

linkages in a synchronized and reversed manner to achieve structures with single crystallinity. While single metal ions have been explored to connect infinite organic species[36,37], often to promote the weaving of 1D organic chains[38–40] and the interlocking of 2D organic layers[41–43], the reticulation of 1D and 2D COFs with well-defined inorganic secondary building units (SBUs)[4] into MOF single crystals has yet to be achieved in the quest for new materials. In essence, to use COFs as building units with infinite connectivity, designing new synthons, deciphering their spatial and topological correlations and formulating bespoke synthetic routes are all indispensable.

Herein we report the synthesis of a series of MOFs featuring 1D and 2D COFs (chains and layers) as the organic components. All repeating units that constitute the COFs have two distinct binding groups (carboxylic acid, pyridyl or boronic acid) at their ends (Fig. 1a), which implement one-to-one selectivity in the reticulation process (Fig. 1b). Boroxine linkages[27,44–46] and their adducts with pyridyl units through dative B←N bonds[47–52] (Fig. 1c) generate in situ 1D and 2D COFs with precisely anchored carboxylate groups extending outward from the chains or the layers. Furthermore, metal–carboxylate coordinative linkages fix the organic infinite chains or layers and Zr_6O_8-based or Hf_6O_8-based SBUs in 3D space (Fig. 1d), giving rise to open frameworks with surface areas up to 2,300 $m^2\ g^{-1}$. Overall, the integration of multiple linkages—each well-established in MOF or COF chemistry—overcomes long-standing limitations in framework design, producing frameworks with structural compartmentalization and anisotropy.

Results and discussion

Synthesis of MOFs from discrete organic units

A solvothermal reaction between Zr(IV) and 4-boronobenzoic acid (BBC) has yielded single crystals of MOF-401 (Supplementary Table 3). Specifically, self-condensation of three BBC molecules forms 4,4′,4″-(1,3,5,2,4,6-trioxatriborinane-2,4,6-triyl)tribenzoic acid ($H_3(B_3O_3)(BC)_3$) with C_3 symmetry (Fig. 2a). This product features a trimeric boroxine (B_3O_3) core and three extending benzoic acid groups as branches, and it can be viewed as a zero-dimensional (0D) three-connected (3-c) linker (named 0D-L1) for reticular synthesis. In the one-pot synthesis, the in situ-formed triangular linkers further connect with 6-c triangular anti-prismatic $[Zr_6O_8]$ units (Fig. 3a) to construct MOF-401 (Extended Data Fig. 1a,b). Overall, MOF-401 can be characterized as threefold interpenetrated (3,6)-connected **spn** nets bridged by formate ions (Fig. 3b and Supplementary Fig. 4). Mechanistically, two formate ions in every Zr_6O_8-based SBU bridge adjacent nets through their coordination to two Zr(IV) ions in the SBU and two boroxine B atoms from two neighbouring nets, resulting in close contact between the bridged nets (Supplementary Fig. 4). Notably, the structure of MOF-401 has been reported as BUT-108 (ref. 53), although in the initial report, the main framework was inadvertently described as a twofold interpenetration.

Similarly, in a reaction between the longer (1,1′-biphenyl)-4-carboxylic acid (BBPC) and Zr(IV), self-condensation of BBPC affords 4′,4‴,4⁗-(1,3,5,2,4,6-trioxatriborinane-2,4,6-triyl)tris(((1,1′-biphenyl)-4-carboxylic acid)) ($H_3(B_3O_3)(BPC)_3$, named 0D-L2), which has the same boroxine core as 0D-L1 but with longer extensions (Fig. 2a). Further reticulation of the triangular 0D-L2 with the same 6-c Zr_6O_8-based SBUs (Fig. 3a) produces MOF-402 (Fig. 3b, Extended Data Fig. 1c,d and Supplementary Table 3). MOF-402 is isostructural with MOF-401, differing only in its fourfold interpenetrated **spn** nets bridged by formate ions (Supplementary Fig. 4).

The acidic B atom in the boroxine is capable of accepting electrons further from donors such as pyridine, and thus the connectivity (number of extension points) of the boroxine unit can be upgraded. In view of this, we introduce 4-pyridineboronic acid (PyBA) with both pyridyl and boronic acid groups to the framework synthesis. In a solvothermal reaction of Zr(IV), BBPC and PyBA, a dative B←N bond forms between the BBPC-based boroxine unit and PyBA, in agreement with the proposed mechanism (Fig. 2b). Overall, eight BBPC and four PyBA molecules are merged into a large 0D octacarboxylic acid linker (denoted as 0D-L3) with square prismatic (D_{4h}) geometry. The core of 0D-L3 is a square with –PyB– as the edges and the boroxine units anchored at the corners. This 8-c linker is further reticulated with the 8-c Zr_6O_8-based unit (Fig. 3a) to afford MOF-403 which has the topology of the **bcu** net (Fig. 3c, Extended Data Fig. 1e,f and Supplementary Table 3). MOF-403 is one of very few Zr-based MOFs with octatopic linkers[54–56]. Furthermore, the organic 0D-L3 linker stands out for its square macrocyclic structure featuring an edge length of 6.0 Å (Fig. 2b), exemplifying the concept of a porous MOF with intrinsically porous linkers.

Synthesis of MOFs from infinite organic units

B←N bonds are known to construct supramolecular polymers or frameworks by designing boronic acid and N donor moieties in the monomer[57–60]. Thus, beyond the discrete boroxine-core linkers (0D-L1, 0D-L2 and 0D-L3), the construction of 1D organic chains and even 2D organic layers as linkers for MOFs is feasible. In the preparation of MOF-404 from BBC, PyBA and Zr(IV), we obtained an infinite 1D organic

https://doi.org/10.1038/s41557-025-01953-2

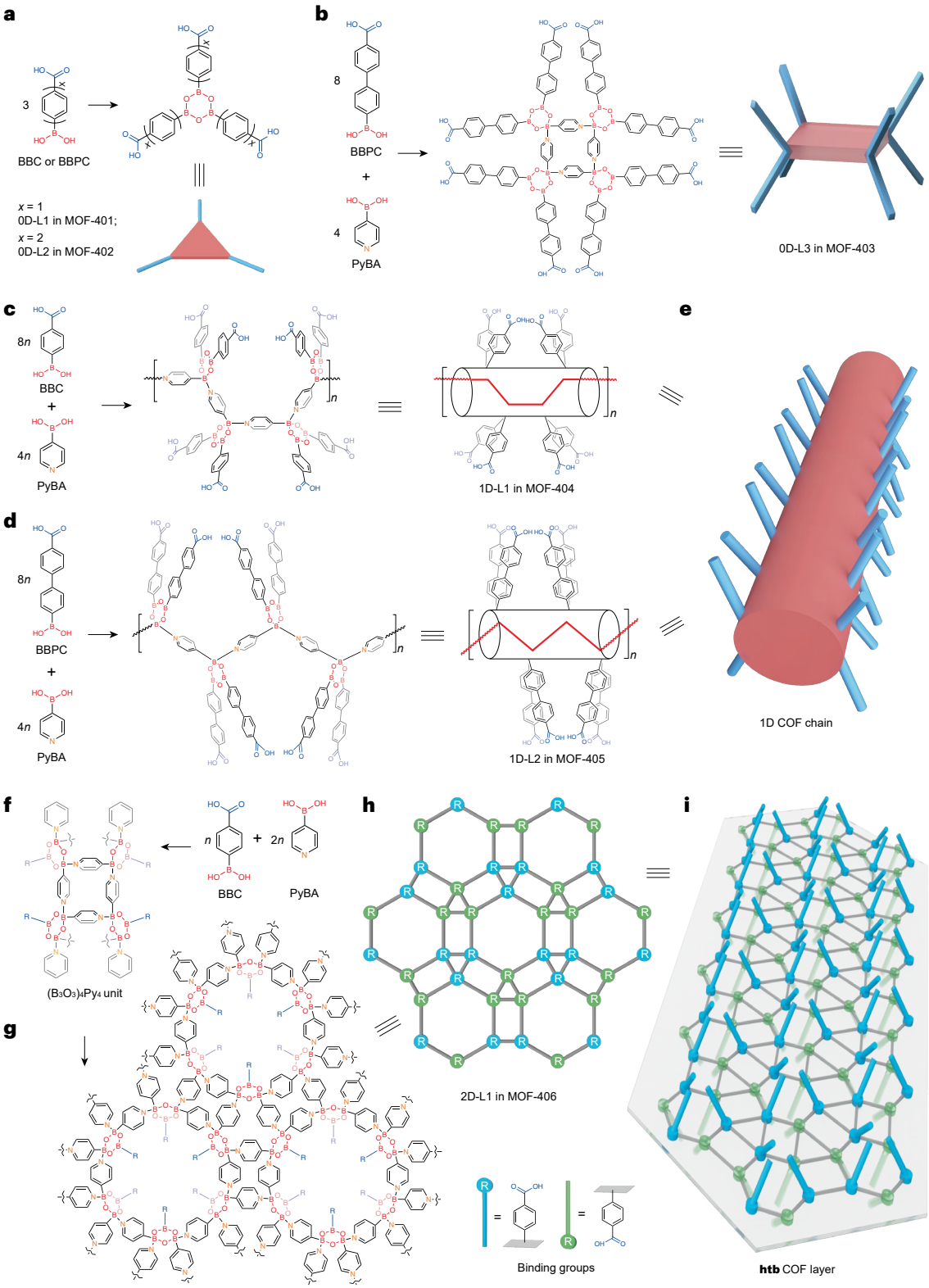

Fig. 2 | 0D, 1D and 2D organic linkers in MOF-401–MOF-406. a, Self-condensation of three BBC or BBPC molecules affords 3-c linkers (0D-L1 and 0D-L2) with trimeric boroxine cores. **b**, Octacarboxylic acid linker (0D-L3) with square prismatic geometry is obtained through the condensation of BBPC and PyBA. **c**,**d**, Infinite 1D organic chains of 1D-L1 (**c**) and 1D-L2 (**d**) are constructed by repeating –PyB– units in the backbones, and they have numerous benzoic acid and 4-biphenylcarboxylic acid groups as the side branches, respectively. **e**, 1D-L1 and 1D-L2 can be regarded as infinite 1D COFs with carboxylic acids pointing outward in four different directions. **f**, Each boroxine linkage in the $(B_3O_3)_4Py_4$ square's corners could be an acceptor for two dative B←N bonds. **g**, The square units are further fused together in a corner-sharing mode to produce 2D-L1. **h**, The layered 2D-L1 is a COF with an **htb** net. **i**, In 2D-L1, benzoic acid groups point upward or downward on both sides as potential docking sites for the metal clusters.

https://doi.org/10.1038/s41557-025-01953-2

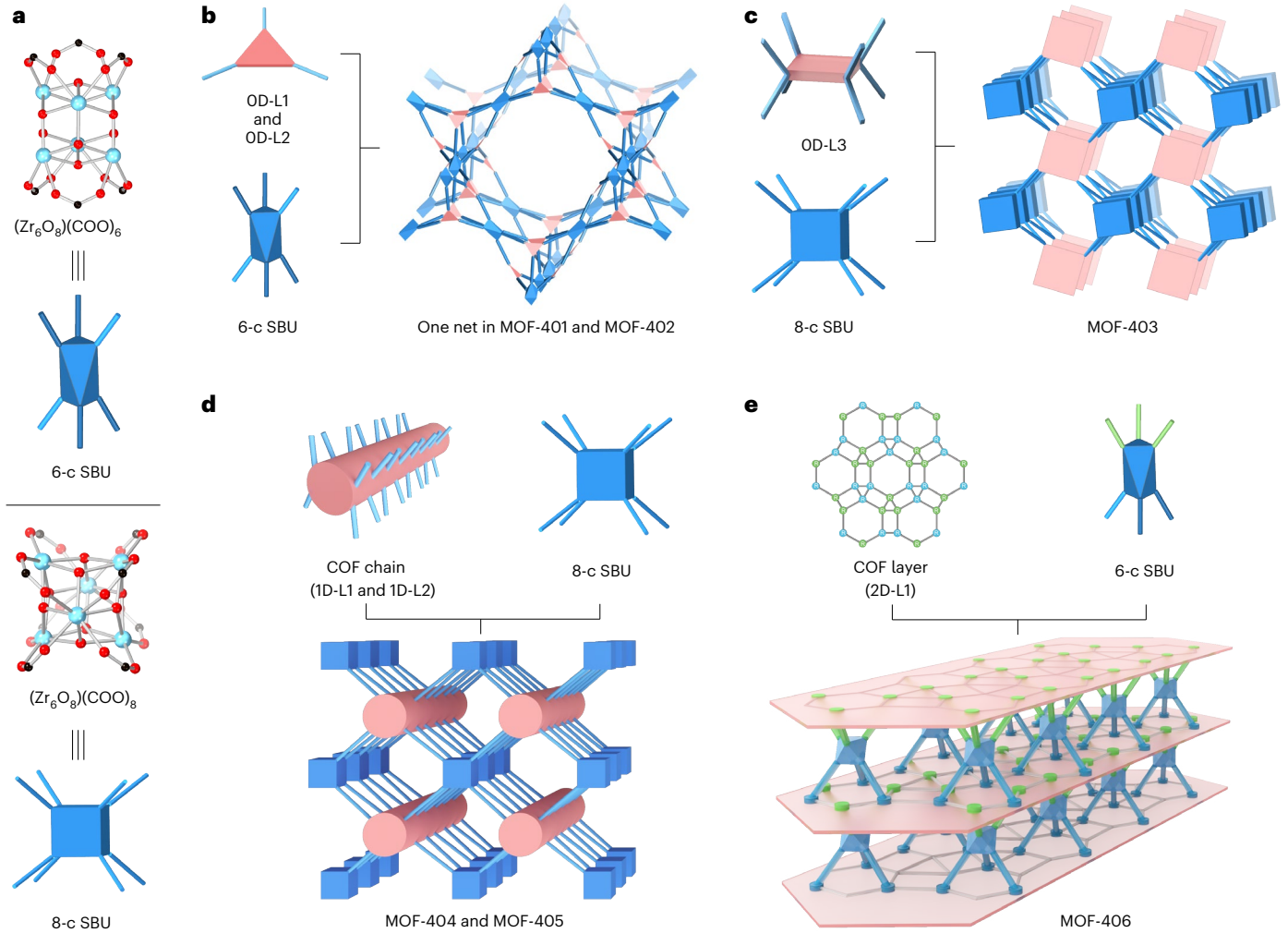

Fig. 3 | Structures of MOF-401–MOF-406 based on the designed 0D, 1D and 2D organic linkers and the Zr_6O_8-based SBUs. a, All MOFs feature Zr_6O_8-based SBUs with a connectivity of six or eight. **b**, MOF-401 and MOF-402 in the topology of the **spn** net are reticulated by the 3-c triangles and the 6-c triangular antiprisms. **c**, MOF-403 in the topology of the **bcu** net is built by alternative arrangement of two kinds of 8-c square prisms. **d**, MOF-404 and MOF-405 feature 1D COF linkers and 8-c inorganic nodes. **e**, Coordination between the 2D COF linkers and the 6-c inorganic nodes creates MOF-406 with a high level of anisotropy.

chain (denoted as 1D-L1) with PyBA as the repeating units and BBC as the side branches (Fig. 2c). The repeating units and the side branches are joined together by the boroxine units. Overall, 1D-L1 can be viewed as infinite rods with numerous carboxylic acid groups pointing outward in four different directions (Fig. 2e). The infinite 1D-L1 and arrays of 8-c Zr_6O_8-based SBUs are joined together to build MOF-404 (Fig. 3d, Extended Data Fig. 2a,b and Supplementary Table 4).

In a similar manner, MOF-405 (Supplementary Table 5) based on another 1D covalent chain (named 1D-L2) is constructed in a reaction of BBPC, PyBA and Zr(IV) (Supplementary Information has a detailed discussion on the solvent choice; Supplementary Table 1). The 1D-L2 features PyBA in its backbone and BBPC as its side branches (Fig. 2d). Before delving into the structural details of MOF-405, we first emphasize that 1D-L1 and 1D-L2 have very different conformations, which are imposed by the spatial configuration of the PyBA monomers in the backbones. The 1D-L1 linker is in an eclipsed conformation (Fig. 2c), while the 1D-L2 linker follows an all-*trans* conformation (Fig. 2d). The difference probably occurs because the bulkier BBPC in 1D-L2 causes the 1D chain to adopt an energetically more favoured all-*trans* conformation. The side branches in 1D-L2 coordinate with $[Zr_6O_8]$ clusters to afford MOF-405 (Fig. 3d and Extended Data Fig. 2c,d), which exhibits an intriguing disordered arrangement of both the side branches and the SBUs within the crystal lattice (Supplementary Fig. 8).

Notably, in all three linkers—including the square prismatic 0D-L3 with one boroxine ring, and the infinite 1D-L1 and 1D-L2 with numerous boroxine rings each—only one B←N bond is observed per boroxine ring. By adjusting the molar ratio of BBC (or BBPC) to PyBA from 2:1 (stoichiometric ratio for MOF-403–MOF-405) to 1:2 (Supplementary Table 2), the pyridyl group concentration in solution was increased. This yielded 2D COF layers (2D-L1, stoichiometry 1:2) featuring two B←N bonds per boroxine unit (Fig. 2f) and enabled the synthesis of MOF-406. Specifically, neighbouring $(B_3O_3)_4Py_4$ squares, which are the same as the core in 0D-L3, are fused together through B←N bonds in a corner-sharing mode. Considering each boroxine as the nodes, the 2D COF (Fig. 2g) could be simplified as a periodic **htb** layer composed of triangles, squares and hexagons (Fig. 2h). The benzoic acid groups, pointing upward or downward, are covalently attached to both sides of the layers with precisely defined positions and orientations (Fig. 2i). By stitching the **htb** layers together with the 6-c Zr_6O_8-based SBUs (Fig. 3a), MOF-406 is constructed (Fig. 3e and Extended Data Fig. 3).

From a synthetic view, in addition to molecular organic linkers, the 1D and 2D linkers allow rational design of infinite organic rods and layers for anisotropic networks. Based on the same boroxine linkages and the B←N bonds, the presented organic linkers feature different geometries (triangular, square prismatic, 1D in eclipsed and all-*trans* conformations and 2D in the topology of the **htb** net), different topicities (3-c, 8-c

https://doi.org/10.1038/s41557-025-01953-2

and infinitely connected) and distinct extension lengths (benzoic acid and biphenyl carboxylic acid). Further reticulation of these linkers with well-defined inorganic SBUs has afforded a platform to include infinite and yet periodic organic components (chains and layers) with specific directionality into porous and robust frameworks.

Spatial compatibility between the infinite linkers and the SBUs

Given that the numerous binding groups in the infinite 1D and 2D linkers are already positioned in an ordered pattern, it is essential to have a high degree of correlation in both geometric and translational symmetry between the units (organic linkers and inorganic SBUs) in the periodic space. For example, the formation of a polynuclear SBU requires multiple –COOH groups to be in exact proximity and to emanate from predetermined directions. If multiple binding groups from one infinite linker are employed to connect with an SBU, the binding groups and the SBU must exhibit spatial compatibility and align in a manner akin to how an electrical plug fits into a socket.

To illustrate the spatial compatibility proposition, we analysed the metrical parameters of MOF-404 made from the infinite 1D-L1 and arrays of 8-c Zr_6O_8-based SBUs. Note that the ideal turning angle between the adjacent repeating –PyB– units (6.0 Å in length based on the optimized molecular structure; Supplementary Fig. 12 shows the measurement based on the crystal structure) in 1D-L1 is ~109°, resulting in a 10.0 Å distance (*d*) between the binding group anchoring points and a 67° binding group raising angle (Fig. 4a and Supplementary Fig. 14). In addition, the binding group length in BBC is 8.3 Å (Supplementary Fig. 13). These metrical parameters contribute a perfect docking between the two –COOH groups and the 8-c Zr_6O_8-based unit (4.5 Å in radius; Supplementary Fig. 11). Indeed, the parameters from the single-crystal structure of MOF-404 show only a slight deviation from the ideal values (Supplementary Figs. 11–14). Overall, the eclipsed conformation of 1D-L1 results in four parallel arrays of SBUs around each infinite organic chain.

Spatial compatibility at its best is demonstrated in MOF-406, in which the 6-c triangular anti-prismatic Zr_6O_8-based SBUs act as two-headed three-pronged plugs that stitch neighbouring 2D COF layers together (Fig. 3e). Although MOF-406 crystallizes only at a micrometre size and is not suitable for in-house single-crystal X-ray diffraction (SXRD) analysis, powder X-ray diffraction (PXRD) confirms that it shares identical unit-cell parameters with its single-crystalline analogue bearing a –F substituent at the 2-positions of BBC (named MOF-406F; Supplementary Figs. 9, 23 and 24 and Supplementary Table 5). Specifically, the 2D-L1 linker in MOF-406 interfaces with each SBU through three binding groups, and thus a mathematical correlation in 3D space is required (Fig. 4b). The inter-anchoring point distance (d = 11.5 Å; Supplementary Fig. 12), binding group raising angle (55°; Supplementary Fig. 14) and binding group length (7.3 Å; Supplementary Fig. 13) are all close to those of the constructed mathematical model. The 2D COF layers function as directional, continuous and periodic organic subnets, and furthermore, the alternating stacks of organic and inorganic layers give rise to anisotropy within the material.

But the successful construction of MOF-405 could not be simply explained by the spatial compatibility. Similar to MOF-404, MOF-405 has 1D linkers connected by arrays of 8-c SBUs. Due to the all-*trans* (zigzag) conformation of the $[PyB]_n$ chain (Supplementary Fig. 12), the raising angle of the binding group is ~90° (Fig. 4c). Bending of the binding groups is necessary for the two initially parallel –COOH groups to touch the same Zr_6O_8-based cluster. The biphenyl carboxylate in BBPC exhibits a greater length compared with the benzoate in BBC, and thus it could provide a 12° bending before it meets the inorganic cluster. Comparing MOF-405 with MOF-404, which share the same repeating backbone units, we observe that the conformation of the infinite organic chains serves as an additional characteristic to influence the structure outcome.

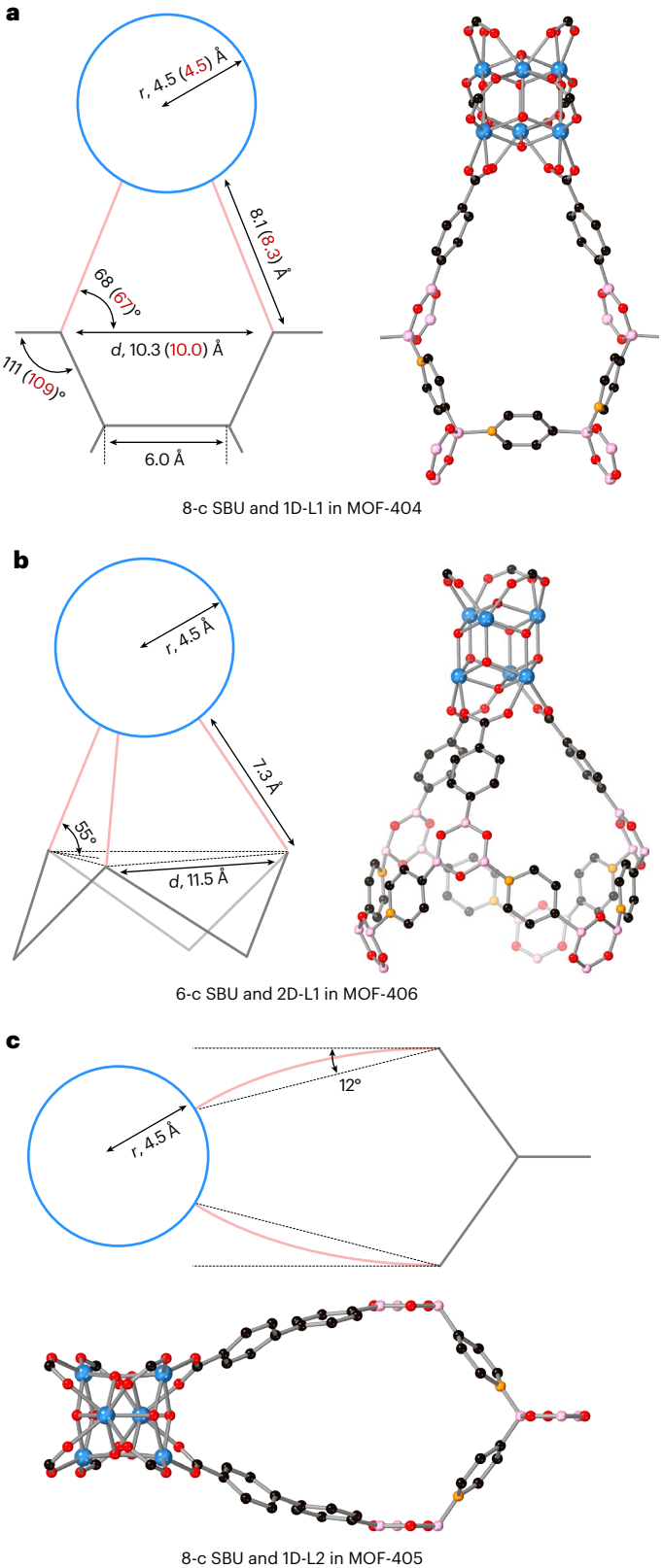

Fig. 4 | The spatial compatibility between the infinite linkers and the SBUs. **a**, The two anchoring points in the 1D-L1 chain in MOF-404 mutually match with the two extending points of the SBU. Metrical parameters obtained from the MOF-404 single-crystal structure (black) and from molecular simulation (red) are presented. *r*, radius. **b**, The three anchoring points in the 2D-L1 layer in MOF-406 fit the three extending points of the SBU. **c**, The binding groups in MOF-405 show a slight bending to assure a successful docking between 1D-L2 and the SBU.

Table 1 | Porosity parameters of the activated MOFs

MOF	Organic unit	Density ($g cm^{-3}$)	BET surface area ($m^2 g^{-1}$)		Pore shape and size		
			Exp.[a]	Theory[b]	Shape	Theoretical size	Major pore size distribution (Exp.)[a]
MOF-401	0D-L1	0.865	1,479	1,956	Cylindrical	Aperture, 10.6 Å	8.6–15.4 Å, centred at 11.5 Å
					Cylindrical	Aperture, 5.2 Å	
MOF-402	0D-L2	0.520	2,435	3,139	Cylindrical	Aperture, 15 Å	9.0–17.0 Å, centred at 11.9 Å
					Cylindrical	Aperture, 8.8 Å	
MOF-403	0D-L3	0.413	1,530	4,249	Interconnected truncated octahedral cage	Major pores, 18×10 Å^2	7.9–11.4 Å (peaks at 8.9 and 10.1 Å, occupying 85% pore volume)
MOF-404	1D-L1	0.687	2,308	2,918	Hexagonal channel	11×9.6 Å^2	8.9–12.5 Å, centred at 10.1 Å
					Rhombic channel	7.0×5.0 Å^2	
MOF-404-*o*F	1D-L1	0.734	2,233	2,780	Hexagonal channel	10.7×9.6 Å^2	8.9–11.0 Å, centred at 9.7 Å
					Rhombic channel	7.0×5.0 Å^2	
MOF-404-*m*F	1D-L1	0.724	2,258	2,783	Hexagonal channel	10.7×9.6 Å^2	8.9–12.4 Å, centred at 10.1 Å
					Rhombic channel	7.0×5.0 Å^2	
MOF-405	1D-L2	0.467	1,380	3,554	Rhombic channel	18×12 Å^2	9.6–16.1 Å, centred at 11.0 Å
					Rhombic channel	12×7.0 Å^2	
MOF-406F	2D-L1	0.666	2,165	2,420	Rhombic channel	14×6.0 Å^2	8.9–14.1 Å, centred at 9.7 Å
					Pseudo-cubic cage	8.0 Å	

Exp., experiment. [a]Supplementary Table 10 contains a full description of the pore size distribution. [b]Accessible surface area modelled by Zeo++.

Synthesis of isoreticular MOFs with COFs as building units

Hafnium, known to form SBUs identical to those in Zr_6O_8-based MOFs, prompted us to explore the synthesis of Hf-based analogues of MOF-401–MOF-405 and MOF-406F (Supplementary Information contains the synthetic methods). As expected, the obtained MOFs, namely MOF-401(Hf)–MOF-405(Hf) and MOF-406F(Hf), are isostructural with their Zr-based analogues; in particular, MOF-401(Hf) was previously reported as BUT-108(Hf) (ref. 53). Structures of MOF-401(Hf), MOF-403(Hf), MOF-404(Hf) and MOF-405(Hf) were determined by SXRD (Supplementary Tables 6 and 7). By contrast, the structures of MOF-402(Hf) and MOF-406F(Hf) were confirmed by comparing their experimental PXRD patterns with those of MOF-402 and MOF-406F, respectively (Supplementary Figs. 26, 30 and 40).

The isoreticular chemistry of MOF-404 was further explored by preparing its analogues with –F attached at the 3- and 2-positions of BBC (4-borono-3-fluorobenzoic acid (3-FBBC) and 4-borono-2-fluorobenzoic acid (2-FBBC), respectively). Crystal structures of the results, named MOF-404-*o*F and MOF-404-*m*F, confirm that they are isoreticular with MOF-404 (Supplementary Figs. 5–7 and Supplementary Table 4). These findings demonstrate the successful extension of isoreticular design principles to MOFs incorporating COFs as the building units, preserving the framework topology while introducing functional variation.

The phase purity of all MOFs—including isoreticular structures based on Hf and those with the –F functionality—is confirmed by PXRD analysis (Supplementary Figs. 17–30). Their Fourier transform infrared spectroscopy, thermogravimetric analysis and chemical stability analysis in various solvents are available in Supplementary Information (Supplementary Figs. 15, 16, 31–39 and 41–46).

Pore analyses of the MOFs

Crystal structures of the MOFs show substantial void spaces inside (Table 1, Extended Data Fig. 4 and Supplementary Table 8). N_2 adsorption isotherms of MOF-401–MOF-405 and MOF-406F all exhibit type-I reversible isotherm characteristics with substantial uptakes in the region of $P/P_0 < 0.05$ (where P is pressure, and P_0 is the saturation vapour pressure of N_2 at 77 K), confirming their microporous nature (Fig. 5a and Supplementary Fig. 47).

The Brunauer–Emmett–Teller (BET) surface areas of MOF-401 and MOF-402 are calculated to be 1,479 and 2,435 $m^2 g^{-1}$ respectively, which are close to, yet slightly lower than, those simulated from the single-crystal structures using Zeo++ software (1,956 and 3,139 $m^2 g^{-1}$) (ref. 61). Although MOF-402 shows a higher fold of interpenetration compared with MOF-401, the extended binding group length indeed enhances the framework porosity. The highly connected MOF-403 shows a BET surface area of 1,530 $m^2 g^{-1}$ that is notably lower than the simulated value (4,249 $m^2 g^{-1}$), although multiple activation methods were attempted (Supplementary Table 9). The discrepancy indicates structural defects in the structure[62,63] (Supplementary Fig. 10 for analysis of possible partial interpenetration). Pore size distribution analysis of MOF-401–MOF-403 (Fig. 5b, Supplementary Fig. 48 and Supplementary Table 10) reveals major micropores with diameters at 8.6–15.4 Å, 9.0–17.0 Å and 7.9–11.4 Å, respectively, and peak maxima centred at 11.5 Å (MOF-401), 11.9 Å (MOF-402) and 8.9 and 10.1 Å (MOF-403). The pore sizes roughly correspond to those obtained from the single-crystal structures (the larger channel with an aperture diameter of 10.6 Å for MOF-401, two kinds of channels with aperture diameters of 15 and 8.8 Å for MOF-402 and interconnected truncated octahedral cages of 18×10 Å^2 for MOF-403; Extended Data Fig. 4a–c).

MOF-404 shows an open architecture with a BET surface area as high as 2,308 $m^2 g^{-1}$ (Fig. 5a). The 1D-L1 linker, with branches extending perpendicularly, divides the space into hexagonal and rhombic channels (Extended Data Fig. 4d). Reflecting its simulated surface area well, MOF-404 shows a pore size of 10.1 Å (Fig. 5b) that is also consistent with the modelled hexagonal channels (11×9.6 Å^2). The rhombic channels feature a diagonal size of merely 7.0×5.0 Å^2 based on the single crystal structure of MOF-404, and therefore the size of these rhombic channels could not be derived from the simulation kernel employed for the collected isotherm.

The presence of longer side branches on the 1D-L2 linker, as opposed to 1D-L1, leads to the formation of hexagonal and rhombic channels that are notably widened in MOF-405. As a result, MOF-405 features channels with theoretical 18×12 Å^2 and 12×7.0 Å^2 openings (Extended Data Fig. 4e). With a 1,380 $m^2 g^{-1}$ BET surface area that is below the expectation (Fig. 5a), the highly disordered MOF-405 displays rather weak PXRD peaks after activation (Supplementary Fig. 22),

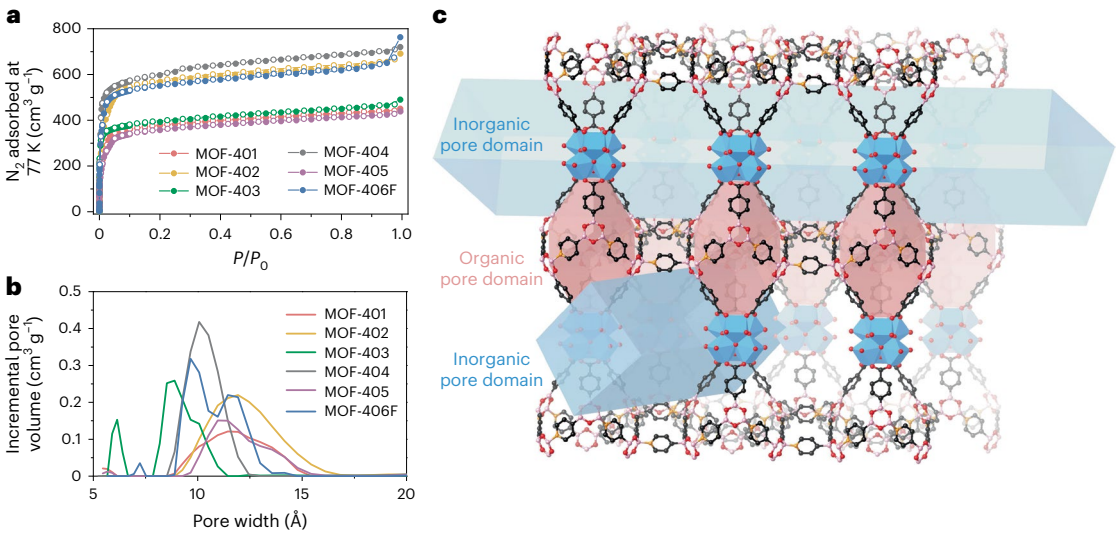

Fig. 5 | Adsorption studies of the MOFs. a, The 77 K N_2 adsorption (filled symbol) and desorption (open symbol) isotherms of MOF-401–MOF-405 and MOF-406F. **b**, Micropore size distribution profiles of MOF-401–MOF-405 and MOF-406F. **c**, MOF-406 features a directional pore domain arrangement because of the alternative packing of inorganic nodes and organic layers.

indicating possible structural deformation due to the long and flexible binding groups anchored on the backbone of 1D-L2.

The alternating arrangement of the 2D-L1 linkers and the Zr_6O_8-based SBUs in MOF-406 and MOF-406F creates two kinds of pore domains that are also alternatively arranged (Fig. 5c and Supplementary Fig. 9). In MOF-406F, the first kind of interconnected rhombic channel is positioned between the SBUs inside the inorganic layer and has a diagonal size of 14 × 6.0 Å^2. The second kind is a pseudo-cubic cage (8.0 Å) inside the organic layer, and six of the corners in its equatorial region are all composed of organic components. Through precise manipulation of COFs and rigid inorganic nodes in an unparalleled manner, MOF-406F has a 2,165 $m^2 g^{-1}$ BET surface area (Fig. 5a). With the diverse structural entities and pore environments organized in separate and yet interconnected sections along specific directions, the open architectures demonstrate structural and pore compartmentalization (Fig. 5c) in solid materials.

MOF-404–MOF-406 introduce a transformative approach to framework chemistry. (1) The approach uses extended covalent architectures to enable structural diversity and complexity in MOFs, thereby creating materials that expand the boundaries of MOFs. (2) Building on the insights and results discussed, future designs incorporating COF units and even carbon materials with high chemical stability and tailored electronic mobility may yield emerging materials with exceptional mechanical, chemical and electronic properties. (3) We anticipate that, with the tremendous ongoing progress of making chemically stable COFs[64], their future use as building units will greatly enhance the structural stability of the overall frameworks. Furthermore, the coexistence of coordination and covalent linkages enables selective bond dissociation[65], whereby cleaving coordinative linkages while preserving organic linkages facilitates synthesizing otherwise inaccessible organic materials.

Conclusion

In summary, a series of framework structures has been synthesized in which infinite covalent rods or layers and well-defined discrete inorganic clusters are integrated within 3D spaces. The strategy combines coordinative linkages and dynamic covalent linkages in a synchronized fashion, thus achieving single crystals with all units in precision. In the frameworks, infinite 1D COF chains in diverse conformations and ordered 2D COF layers with specific topology, possessing boroxine and dative B←N bonds, exhibit a plug–socket match with the Zr_6O_8-based inorganic clusters. These findings underscore the importance of spatial compatibility for designing multicomponent structures. The frameworks show a high level of control of pore size and environment through the application of reticular chemistry. What is more, they feature the compartmentalization of organic and inorganic domains, which is reflected in a heterogeneous and directional arrangement of pores. The presented materials emphasize the concept of COFs as building units for reticular synthesis and substantially broaden the boundaries of MOFs, inspiring future developments to integrate the best from both regimes.

Online content

Any methods, additional references, Nature Portfolio reporting summaries, source data, extended data, supplementary information, acknowledgements, peer review information; details of author contributions and competing interests; and statements of data and code availability are available at https://doi.org/10.1038/s41557-025-01953-2.

References

1. Yaghi, O. M., Kalmutzki, M. J. & Diercks, C. S. *Introduction to Reticular Chemistry* (Wiley-VCH, 2019).
2. Furukawa, H., Cordova, K. E., O'Keeffe, M. & Yaghi, O. M. The chemistry and applications of metal–organic frameworks. *Science* **341**, 1230444 (2013).
3. Slater, A. G. & Cooper, A. I. Function-led design of new porous materials. *Science* **348**, aaa8075b (2015).
4. Kalmutzki, M. J., Hanikel, N. & Yaghi, O. M. Secondary building units as the turning point in the development of the reticular chemistry of MOFs. *Sci. Adv.* **4**, eaat9180 (2018).
5. Geng, K. et al. Covalent organic frameworks: design, synthesis, and functions. *Chem. Rev.* **120**, 8814–8933 (2020).
6. Yaghi, O. & Li, H. Hydrothermal synthesis of a metal–organic framework containing large rectangular channels. *J. Am. Chem. Soc.* **117**, 10401–10402 (1995).
7. Li, H., Eddaoudi, M., O'Keeffe, M. & Yaghi, O. M. Design and synthesis of an exceptionally stable and highly porous metal–organic framework. *Nature* **402**, 276–279 (1999).
8. Kitagawa, S., Kitaura, R. & Noro, S. Functional porous coordination polymers. *Angew. Chem. Int. Ed.* **43**, 2334–2375 (2004).
9. Férey, G. et al. A chromium terephthalate-based solid with unusually large pore volumes and surface area. *Science* **309**, 2040–2042 (2005).

10. Zhang, J.-P., Zhang, Y.-B., Lin, J.-B. & Chen, X.-M. Metal azolate frameworks: from crystal engineering to functional materials. *Chem. Rev.* **112**, 1001–1033 (2011).
11. Li, B. et al. Emerging multifunctional metal–organic framework materials. *Adv. Mater.* **28**, 8819–8860 (2016).
12. Yuan, S. et al. Stable metal–organic frameworks: design, synthesis, and applications. *Adv. Mater.* **30**, 1704303 (2018).
13. Jiang, H., Alezi, D. & Eddaoudi, M. A reticular chemistry guide for the design of periodic solids. *Nat. Rev. Mater.* **6**, 466–487 (2021).
14. Cheetham, A. K., Rao, C. N. R. & Feller, R. K. Structural diversity and chemical trends in hybrid inorganic–organic framework materials. *Chem. Commun*. **2006**, 4780–4795 (2006).
15. Serre, C. et al. Very large breathing effect in the first nanoporous chromium(III)-based solids: MIL-53 or $Cr^{III}(OH)\cdot\{O_2C–C_6H_4–CO_2\}\cdot\{HO_2C–C_6H_4–CO_2H\}_x\cdot H_2O_y$. *J. Am. Chem. Soc.* **124**, 13519–13526 (2002).
16. Guillou, N., Livage, C., Beek, W., Noguès, M. & Férey, G. A layered nickel succinate with unprecedented hexanickel units: structure elucidation from powder-diffraction data, and magnetic and sorption properties. *Angew. Chem. Int. Ed.* **42**, 643–647 (2003).
17. Vaidhayanathan, R., Natarajan, S. & Rao, C. N. R. Aliphatic dicarboxylates with three-dimensional metal–organic frameworks possessing hydrophobic channels. *Dalton Trans*. **2003**, 1459–1464 (2003).
18. Shyu, E. & LaDuca, R. L. Divalent metal succinate/perchlorate coordination polymers incorporating a kinked hydrogen bonding capable diimine: chains, layers and a (5,6)-connected binodal network featuring alternating rectangular and hexagonal grids. *Polyhedron* **28**, 826–834 (2009).
19. Zhang, L. et al. Synthesis, structure, and luminescent properties of hybrid inorganic–organic framework materials formed by lead aromatic carboxylates: inorganic connectivity variation from 0D to 3D. *Inorg. Chem.* **48**, 6517–6525 (2009).
20. Schoedel, A., Li, M., Li, D., O'Keeffe, M. & Yaghi, O. M. Structures of metal–organic frameworks with rod secondary building units. *Chem. Rev.* **116**, 12466–12535 (2016).
21. Smolders, S. et al. A titanium(IV)-based metal–organic framework featuring defect-rich Ti-O sheets as an oxidative desulfurization catalyst. *Angew. Chem. Int. Ed.* **58**, 9160–9165 (2019).
22. Noa, F. M. A. et al. A unified topology approach to dot-, rod-, and sheet-MOFs. *Chem* **7**, 2491–2512 (2021).
23. Jia, H., Han, Q., Luo, W., Cong, H. & Deng, H. Sequence control of metals in MOF by coordination number precoding for electrocatalytic oxygen evolution. *Chem Catal.* **2**, 84–101 (2022).
24. Sun, C., Xi, R. & Fei, H. Organolead halide-based coordination polymers: intrinsic stability and photophysical applications. *Acc. Chem. Res.* **56**, 452–461 (2023).
25. Zhang, W. et al. Metal-halide porous framework superlattices. *Nature* **638**, 418–424 (2025).
26. Shimizu, G. K. H., Vaidhyanathan, R. & Taylor, J. M. Phosphonate and sulfonate metal organic frameworks. *Chem. Soc. Rev.* **38**, 1430–1449 (2009).
27. Côté, A. P. et al. Porous, crystalline, covalent organic frameworks. *Science* **310**, 1166–1170 (2005).
28. Diercks, C. S. & Yaghi, O. M. The atom, the molecule, and the covalent organic framework. *Science* **355**, eaal1585 (2017).
29. Han, X. et al. Chiral covalent organic frameworks: design, synthesis and property. *Chem. Soc. Rev.* **49**, 6248–6272 (2020).
30. Zhang, W. et al. Reconstructed covalent organic frameworks. *Nature* **604**, 72–79 (2022).
31. Han, J. et al. Fast growth of single-crystal covalent organic frameworks for laboratory x-ray diffraction. *Science* **383**, 1014–1019 (2024).
32. Yin, Y. et al. Ultrahigh-surface area covalent organic frameworks for methane adsorption. *Science* **386**, 693–696 (2024).
33. Wang, Z. et al. Flux synthesis of two-dimensional covalent organic frameworks. *Nat. Protoc.* **19**, 3489–3519 (2024).
34. Chen, F. et al. Exploring high-connectivity three-dimensional covalent organic frameworks: topologies, structures, and emerging applications. *Chem. Soc. Rev.* **54**, 484–514 (2025).
35. Li, Y. et al. Integration of metal–organic frameworks and covalent organic frameworks: design, synthesis, and applications. *Matter* **4**, 2230–2265 (2021).
36. Lv, S. et al. Metal–coordinated covalent organic frameworks as advanced bifunctional hosts for both sulfur cathodes and lithium anodes in lithium-sulfur batteries. *J. Am. Chem. Soc.* **146**, 9385–9394 (2024).
37. Endo, K. et al. Crystalline porous frameworks based on double extension of metal–organic and covalent organic linkages. *Nat. Synth.* **4**, 603–613 (2025).
38. Liu, Y. et al. Weaving of organic threads into a crystalline covalent organic framework. *Science* **351**, 365–369 (2016).
39. Zhao, Y. et al. A synthetic route for crystals of woven structures, uniform nanocrystals, and thin films of imine covalent organic frameworks. *J. Am. Chem. Soc.* **139**, 13166–13172 (2017).
40. Xu, H.-S. et al. Single crystal of a one-dimensional metallo-covalent organic framework. *Nat. Commun.* **11**, 1434 (2020).
41. Lu, H.-S. et al. A 3D anionic metal covalent organic framework with soc topology built from an octahedral Ti^{IV} complex for photocatalytic reactions. *Angew. Chem. Int. Ed.* **60**, 17881–17886 (2021).
42. Han, W.-K. et al. Targeted construction of a three-dimensional metal covalent organic framework with spn topology for photocatalytic hydrogen peroxide production. *Chem. Eng. J.* **449**, 137802 (2022).
43. Han, W.-K. et al. Integrating light-harvesting ruthenium(II)-based units into three-dimensional metal covalent organic frameworks for photocatalytic hydrogen evolution. *Angew. Chem. Int. Ed.* **61**, e202208791 (2022).
44. Koricha, A. L. & Iovine, P. M. Boroxine chemistry and applications: a perspective. *Dalton Trans.* **39**, 1423–1431 (2010).
45. Zhan, G. et al. Observing polymerization in 2D dynamic covalent polymers. *Nature* **603**, 835–840 (2022).
46. Preuss, M. D. et al. Functionalization of supramolecular polymers by dynamic covalent boroxine chemistry. *Angew. Chem. Int. Ed.* **63**, e202402644 (2024).
47. Torres-Huerta, A. et al. Structural induction via solvent variation in assemblies of triphenylboroxine and piperazine—potential application as self-assembly molecular sponge. *Cryst. Growth Des.* **17**, 2438–2452 (2017).
48. Ono, K. et al. Dynamic interconversion between boroxine cages based on pyridine ligation. *Angew. Chem. Int. Ed.* **57**, 3113–3117 (2018).
49. Bhandary, S., Shukla, R. & Hecke, K. V. Effect of chemical substitution on the construction of boroxine-based supramolecular crystalline polymers featuring B←N dative bonds. *CrystEngComm* **24**, 1695–1699 (2022).
50. Wang, W. et al. Dative B←N bonds based crystalline organic framework with permanent porosity for acetylene storage and separation. *Chem. Sci.* **14**, 533–539 (2023).
51. Li, Y. et al. Self-healing B←N-based hydrogen-bonded organic framework for exclusive recognition and separation of toluene from methyl-cyclohexane. *J. Am. Chem. Soc.* **146**, 19425–19433 (2024).
52. Xu, J. et al. Visible light-responsive crystalline B←N host adducts with solvent-induced allosteric effect for guest release. *Angew. Chem. Int. Ed.* **63**, e202411880 (2024).
53. Kong, X.-J. et al. Constructing new metal–organic frameworks with complicated ligands from "one-pot" *in situ* reactions. *Chem. Sci.* **10**, 3949–3955 (2019).

54. Liu, W. et al. Reticular synthesis of metal–organic frameworks by 8-connected quadrangular prism ligands for water harvesting. *Angew. Chem. Int. Ed.* **62**, e202305144 (2023).
55. Ortín-Rubio, B. et al. A mesoporous Zr-based metal–organic framework driven by the assembly of an octatopic linker. *Chem. Commun.* **59**, 7803–7806 (2023).
56. Gong, W. et al. Modulator-dependent dynamics synergistically enabled record SO_2 uptake in Zr(IV) metal–organic frameworks based on pyrene-cored molecular quadripod ligand. *J. Am. Chem. Soc.* **145**, 26890–26899 (2023).
57. Sheepwash, E. et al. Molecular networks based on dative boron–nitrogen bonds. *Angew. Chem. Int. Ed.* **50**, 3034–3037 (2011).
58. Zhao, Z.-H., Li, C.-H. & Zuo, J.-L. Dynamic polymeric materials based on reversible B–O bonds with dative boron-nitrogen coordination. *SmartMat* **4**, e1187 (2023).
59. Xiao, X. et al. Formation of polyrotaxane crystals driven by dative boron–nitrogen bonds. *Sci. Adv.* **9**, eadi1169 (2023).
60. Chen, B. & Jäkle, F. Boron-nitrogen Lewis pairs in the assembly of supramolecular macrocycles, molecular cages, polymers, and 3D materials. *Angew. Chem. Int. Ed.* **63**, e202313379 (2024).
61. Willems, T. F. et al. Algorithms and tools for high-throughput geometry-based analysis of crystalline porous materials. *Microporous Mesoporous Mater.* **149**, 134–141 (2012).
62. Walton, K. S. & Snurr, R. Q. Applicability of the BET method for determining surface areas of microporous metal–organic frameworks. *J. Am. Chem. Soc.* **129**, 8552–8556 (2007).
63. Yang, S. et al. A partially interpenetrated metal–organic framework for selective hysteretic sorption of carbon dioxide. *Nat. Mater.* **11**, 710–716 (2012).
64. Haase, F. & Lotsch, B. V. Solving the COF trilemma: towards crystalline, stable and functional covalent organic frameworks. *Chem. Soc. Rev.* **49**, 8469–8500 (2020).
65. Li, X. et al. An imine-linked metal–organic framework as a reactive oxygen species generator. *Angew. Chem. Int. Ed.* **60**, 2534–2540 (2021).

Publisher's note Springer Nature remains neutral with regard to jurisdictional claims in published maps and institutional affiliations.

Springer Nature or its licensor (e.g. a society or other partner) holds exclusive rights to this article under a publishing agreement with the author(s) or other rightsholder(s); author self-archiving of the accepted manuscript version of this article is solely governed by the terms of such publishing agreement and applicable law.

© The Author(s), under exclusive licence to Springer Nature Limited 2025

Methods

Synthesis of MOF-401

$ZrCl_4$ (4.7 mg, 0.02 mmol) and BBC (6.6 mg, 0.04 mmol) are dissolved in a mixture of 1.0 ml *N*,*N*-dimethylformamide (DMF) and 90 µl formic acid in a 10 ml glass vial. The vial is capped tightly and placed in an oven at 110 °C for 72 h, and colourless polyhedral crystals are obtained. After cooling to room temperature, the crystals are collected and rinsed with fresh DMF, three times. The crystals are then solvent-exchanged with acetone for three days, during which the solvent exchanges are performed three times per day. The acetone-exchanged sample is activated at 60 °C under vacuum for 12 h. The yield is 3.9 mg.

Synthesis of MOF-402

$ZrCl_4$ (4.7 mg, 0.02 mmol) and BBPC (9.6 mg, 0.04 mmol) are dissolved in a mixture of 0.5 ml DMF, 0.5 ml CH_3CN, 0.3 ml toluene and 90 µl formic acid in a 10 ml glass vial. The vial is capped tightly and placed in an oven at 110 °C for 72 h, and colourless rodlike crystals are obtained. The crystals are collected after cooling and rinsed with fresh DMF, three times. The crystals are then solvent-exchanged with CH_3CN for three days, during which the solvent exchanges are performed three times per day. The CH_3CN-exchanged sample is activated at room temperature under vacuum for 12 h. The yield is 3.9 mg.

Synthesis of MOF-403

$ZrCl_4$ (4.7 mg, 0.02 mmol), BBPC (9.6 mg, 0.04 mmol) and PyBA (2.5 mg, 0.02 mmol) are dissolved in a mixture of 1.0 ml toluene, 0.5 ml CH_3CN, 0.4 ml *N*-methylformamide (NMF) and 80 µl formic acid in a 10 ml glass vial. The vial is capped tightly and placed in an oven at 110 °C for 48 h, and colourless block crystals are obtained. The same solvent exchange and activation procedures as with MOF-402 are applied to the NMF-rinsed MOF-403. The yield is 5.9 mg.

Synthesis of MOF-404

$ZrCl_4$ (4.7 mg, 0.02 mmol), BBC (6.6 mg, 0.04 mmol) and PyBA (2.5 mg, 0.02 mmol) are dissolved in a mixture of 1.5 ml CH_3CN, 1.0 ml DMF and 110 µl formic acid in a 10 ml glass vial. The vial is capped tightly and placed in an oven at 120 °C for 48 h, and colourless block crystals are obtained. The same rinse and solvent exchange procedures as with MOF-401 are applied. The acetone-exchanged MOF-404 is activated at room temperature under vacuum for 12 h. The yield is 5.4 mg.

Synthesis of MOF-404-*o*F

The synthesis recipe of MOF-404-*o*F is similar to the preparation of MOF-404, except that the BBC is replaced by 3-FBBC (7.2 mg, 0.04 mmol). The same rinse and solvent exchange procedures as with MOF-401 are applied. The acetone-exchanged sample is activated at 80 °C under vacuum for 12 h. The yield is 6.2 mg.

Synthesis of MOF-404-*m*F

The synthesis procedure and solvent exchange of MOF-404-*m*F is based on those of MOF-404-*o*F, with 2-FBBC (7.2 mg, 0.04 mmol) replacing 3-FBBC. The acetone-exchanged sample is activated at 60 °C under vacuum for 12 h. The yield is 6.6 mg.

Synthesis of MOF-405

$ZrCl_4$ (4.7 mg, 0.02 mmol), BBPC (9.6 mg, 0.04 mmol) and PyBA (2.5 mg, 0.02 mmol) are dissolved in a mixture of 1.0 ml *N*,*N*-diethylformamide (DEF), 1.0 ml CH_3CN and 110 µl formic acid in a 10 ml glass vial. The vial is capped tightly and placed in an oven at 110 °C for 48 h, and colourless block crystals are obtained. The same rinse and solvent exchange procedures as with MOF-401 are applied. The acetone-exchanged sample is activated at room temperature under vacuum for 12 h. The yield is 5.7 mg.

Synthesis of MOF-406

$ZrCl_4$ (4.7 mg, 0.02 mmol), BBC (3.3 mg, 0.02 mmol) and PyBA (5.0 mg, 0.04 mmol) are dissolved in a mixture of 1.0 ml NMF, 1.0 ml CH_3CN and 120 µl formic acid in a 10 ml glass vial. The vial is capped tightly and placed in an oven at 120 °C for 24 h, and colourless crystals are obtained. The yield is 4.9 mg.

Synthesis of MOF-406F

$ZrCl_4$ (4.7 mg, 0.02 mmol), 2-FBBC (3.6 mg, 0.02 mmol) and PyBA (5.0 mg, 0.04 mmol) are dissolved in a mixture of 1.0 ml NMF, 1.0 ml CH_3CN and 150 µl formic acid in a 10 ml glass vial. The vial is capped tightly and placed in an oven at 120 °C for 24 h, and colourless rodlike crystals are obtained. The NMF-washed crystals are solvent-exchanged with acetone for three days, during which the solvent exchanges are performed three times per day, followed by activation at room temperature under vacuum for 12 h. The yield is 6.0 mg.

Data availability

All data that support the findings of this study are available in the paper and its Supplementary Information. X-ray crystallographic data for the structures reported in this article have been deposited at the Cambridge Crystallographic Data Centre (CCDC) under deposition numbers 2416824 (for MOF-401), 2416825 (for MOF-402), 2416826 (for MOF-403), 2416827 (for MOF-404), 2416828 (for MOF-404-*o*F), 2416829 (for MOF-404-*m*F), 2416830 (for MOF-405), 2416831 (for MOF-406F), 2457479 (for MOF-401(Hf)), 2457480 (for MOF-403(Hf)), 2457481 (for MOF-404(Hf)) and 2457482 (for MOF-405(Hf)). Copies of the data can be obtained free of charge via https://www.ccdc.cam.ac.uk/structures/. Source data are provided with this paper.

Acknowledgements

This work was supported by the National Key Research and Development Program of China (grants 2018YFA0209401 and 2021YFA1500400), the National Natural Science Foundation of China (grants 21922103, 21961132003, 22088101, 22331009 and U22A20401) and the Science and Technology Commission of Shanghai Municipality (grant 2024ZDSYS02). We thank L. Hou, Z. Jiang and Y. Rao for their assistance with the structure refinement and illustration.

Author contributions

B.L., H.-L.J. and Q.L. conceived the project. H.-L.J. and Q.L. supervised the project. B.L. designed and performed the syntheses. B.L. and Y.W. performed the structure characterizations and porosity studies. L.W. also performed the syntheses. B.L., Y.W., H.-L.J. and Q.L. wrote the paper. All authors contributed to the data analysis, discussion and revision of the paper.

Competing interests

The authors declare no competing interests.

Additional information

Extended data is available for this paper at https://doi.org/10.1038/s41557-025-01953-2.

Supplementary information The online version contains supplementary material available at https://doi.org/10.1038/s41557-025-01953-2.

Correspondence and requests for materials should be addressed to Hai-Long Jiang or Qiaowei Li.

Peer review information *Nature Chemistry* thanks Shuhei Furukawa and Fernando Uribe-Romo for their contribution to the peer review of this work.

Reprints and permissions information is available at www.nature.com/reprints.

https://doi.org/10.1038/s41557-025-01953-2

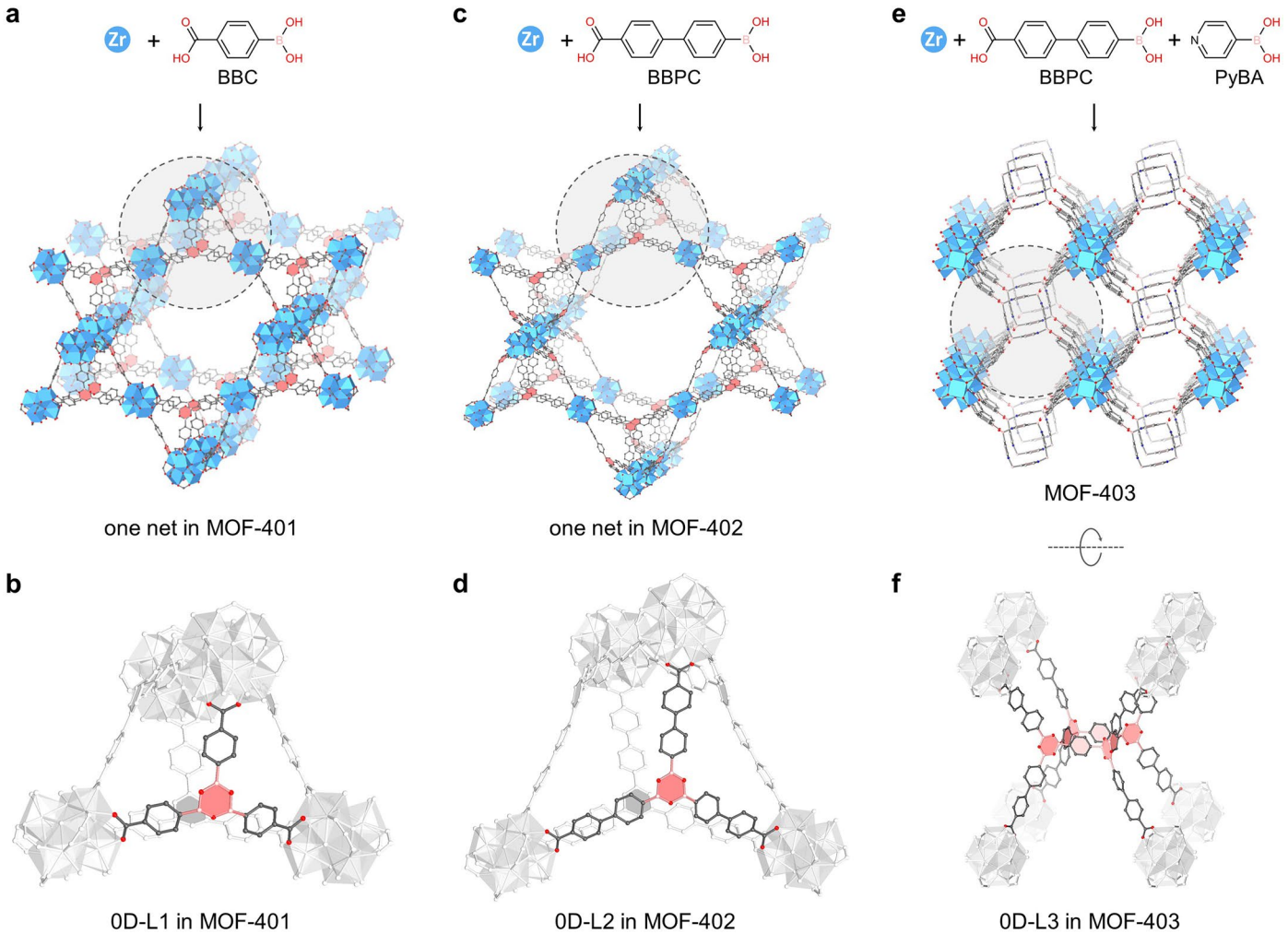

Extended Data Fig. 1 | Structures of MOF-401–403. Single crystal structures of MOF-401 (**a**) and MOF-402 (**c**), each depicting one **spn** net, and the structure of MOF-403 (**e**). The corresponding linkers, 0D-L1 (**b**), 0D-L2 (**d**), and 0D-L3 (**f**), are highlighted with their cores colored pink. Blue polyhedra represent Zr. Grey, red, and pink spheres represent C/N, O, and B atoms, respectively.

https://doi.org/10.1038/s41557-025-01953-2

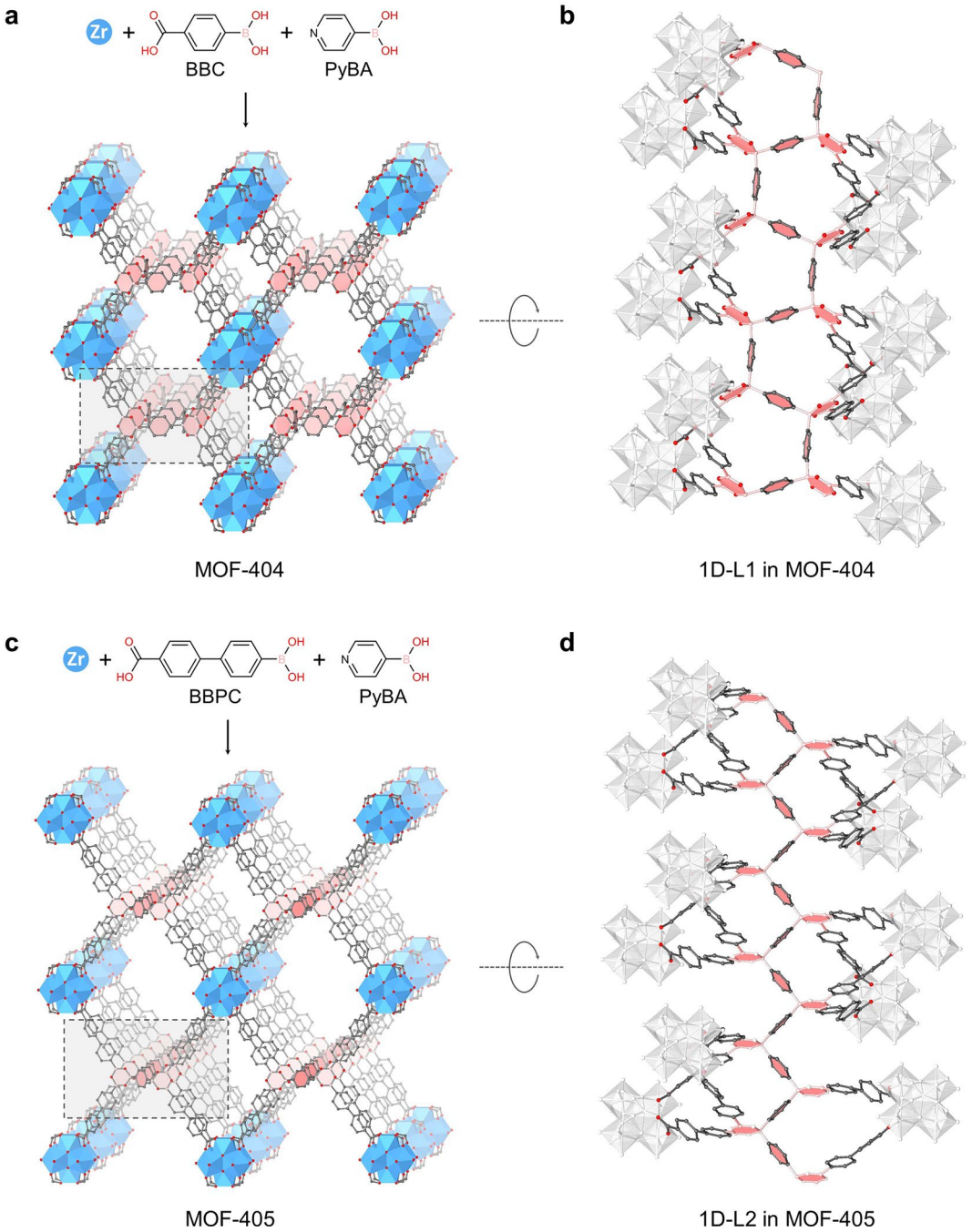

Extended Data Fig. 2 | Structures of MOF-404 and MOF-405. Single crystal structures of MOF-404 (**a**) and MOF-405 (**c**), and their corresponding linkers 1D-L1 (**b**) and 1D-L2 (**d**). B_3O_3 and pyridyl rings are colored pink. Blue polyhedra represent Zr. Grey, red, and pink spheres represent C/N, O, and B atoms, respectively.

https://doi.org/10.1038/s41557-025-01953-2

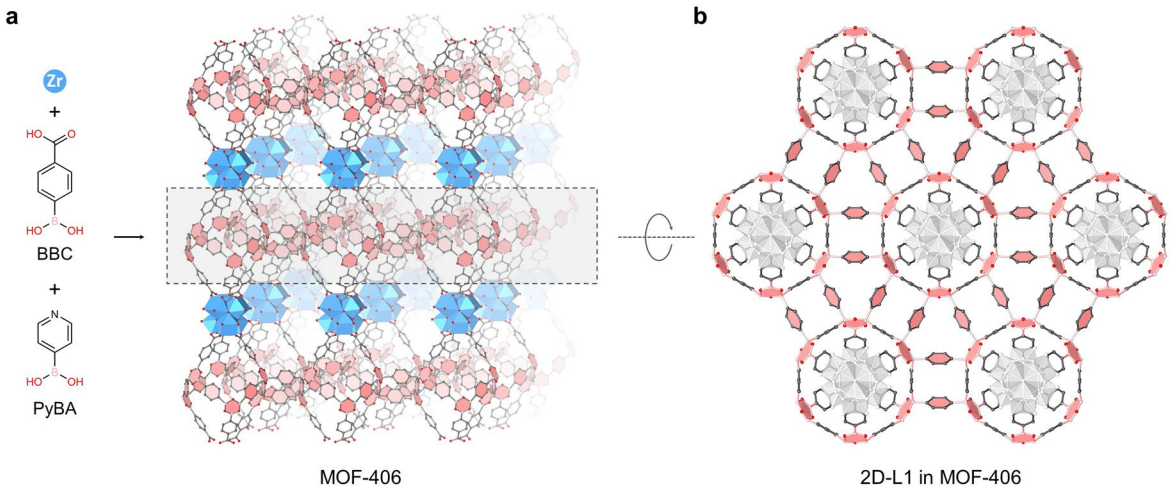

Extended Data Fig. 3 | Structure of MOF-406. Extended structure of MOF-406 (**a**) and its corresponding linker 2D-L1 (**b**). B_3O_3 and pyridyl rings are colored pink. Blue polyhedra represent Zr. Grey, red, and pink spheres represent C/N, O, and B atoms, respectively.

https://doi.org/10.1038/s41557-025-01953-2

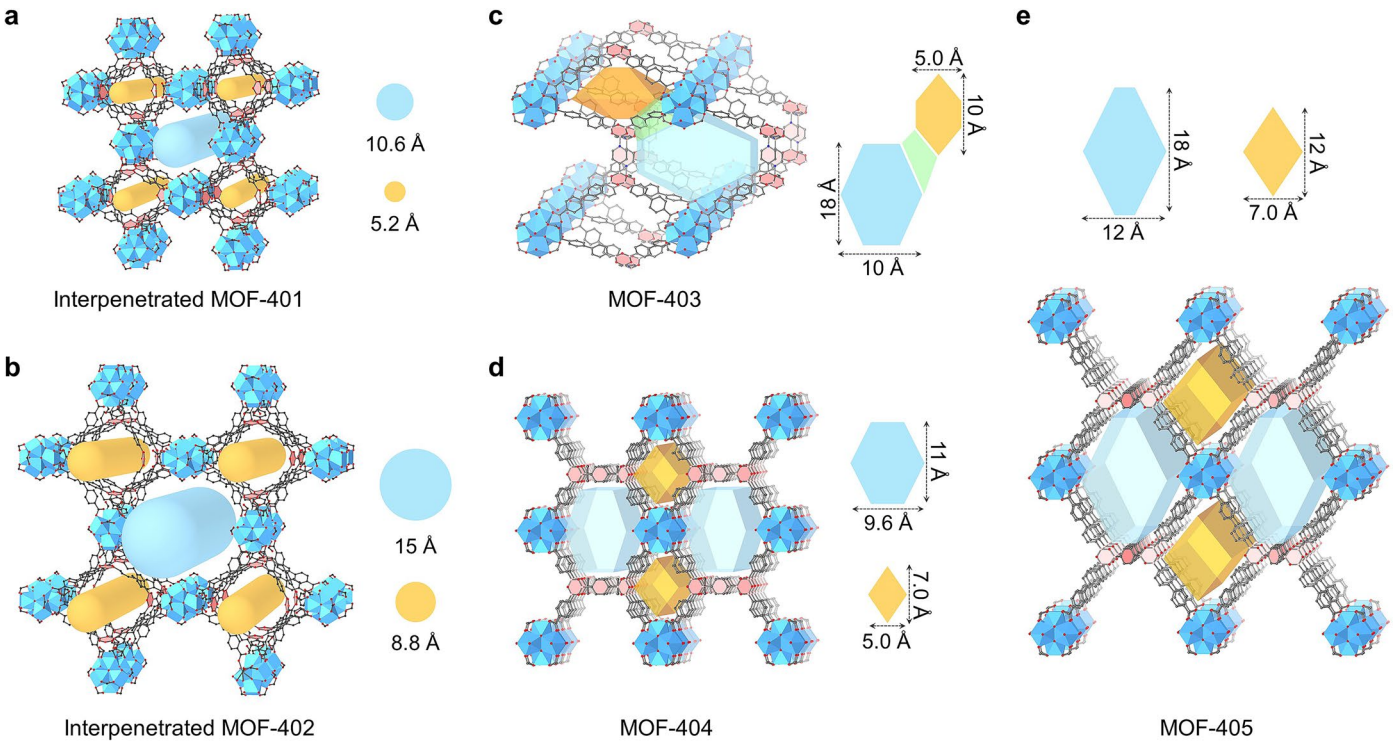

Extended Data Fig. 4 | Pore size and shape illustration of MOF-401–405. Interpenetrated MOF-401 (**a**) and MOF-402 (**b**) exhibit cylindrical pore channels; MOF-403 (**c**) contains two interconnected cage types; and each of MOF-404 (**d**) and MOF-405 (**e**) features two kinds of prismatic channels.